Effect of Nitrogen on the Amorphous Structure and Subthreshold Electrical Conduction of GeSeSb-Based Ovonic Threshold Switching Thin Films

Anthonin Verdy,* Francesco d'Acapito, Jean-Baptiste Dory, Gabriele Navarro,* Mathieu Bernard, and Pierre Noé*

Herein, the amorphous structure of Ge–Se–Sb–N chalcogenide thin films is investigated through Raman, infrared, and X-ray absorption spectroscopies in the light of the electrical performances of such materials once integrated in ovonic threshold switching (OTS) selector devices. In particular, it is shown that the presence of homopolar and wrong bonds in the amorphous structure has a detrimental impact on the subthreshold leakage current of the OTS devices. Although the presence of Sb–Sb and Ge–Sb bonds tends to increase the leakage current in pristine devices, the presence of Se–Se bonds is correlated to a significant device-to-device dispersion of subthreshold characteristics after the device initialization. Finally, the incorporation of a proper N concentration in Ge–Se–Sb glass permits to suppress the homopolar bonds, leading to a very low leakage current and a low device-to-device dispersion.

Resistive crossbar arrays represent nowadays a valuable solution for the design of innovative memory systems for storage class memory applications. In this architecture, the memory element is located at the intersection of the word lines and the bit lines.[1] Such a parallelism induces the inherent creation of sneak paths and leakage currents (I_{leak}) that can induce cell-to-cell disturbances upon programming, as well as failure in cell reading. Therefore, each resistive memory cell (1R) of the crossbar array requires to be integrated in the back end of line (BEOL) in series with a BEOL selector (1S) to form a so-called 1S1R device. The BEOL selector device has the function to replace the commonly used selection made by a transistor. Among the different BEOL selector technologies that are studied in the literature, the one based on ovonic threshold switching (OTS) materials represents one of the best and most promising technological solution, as demonstrated by the recent commercialization of the Optane memory by Intel and the intense research and developments around OTS in the last years.[2–10]

OTS materials are amorphous chalcogenide exhibiting the unique property, upon electric-field application, to switch from a highly resistive state, the OFF-state, to a metastable conductive state, the ON-state, when the applied voltage exceeds the threshold voltage V_{th}.[11] When the ON-state current is decreased below the holding current I_h, the material recovers its highly resistive OFF-state. A typical current–voltage characteristic of an OTS device is shown in **Figure 1**a. The OFF-state is responsible for the leakage current in unselected cells, whereas the ON-state is used for the programming and the reading operations of the memory device.

OTS selectors have to fill different requirements that depend also on the electrical parameters of the memory element. It should ensure an optimized threshold voltage to limit unwanted switching events, a threshold current compatible with the cointegrated resistive memory, a low leakage current I_{leak} (i.e., low OFF-state current), and a thermal stability compatible with CMOS BEOL integration for which the material could typically experience a thermal stress of about 400 °C.[12] Most of the OTS materials that fulfill all these specifications are chalcogenide glasses composed by one or more chalcogen elements, in general Se and/or Te, glass former elements such as Ge, Si, or As and sometimes light dopant atoms such as N or C atoms. Thus, OTS materials are quite complex amorphous materials and the control of their structure and of their properties becomes a key challenge for applications.

In this article, by means of the material engineering of Ge–Se–Sb–N system, we evidence the link between the local order in the amorphous structure of OTS materials, investigated by Raman, infrared, and extended X-ray absorption fine structure (EXAFS) spectroscopies, and the subthreshold current behavior when integrated in selector devices. Despite Sb incorporation in Ge–Se films allows to significantly decrease the threshold voltage of such glasses,[13] it exhibits the major hindering drawback of decreasing the thermal stability against undesired crystallization, leading also to a detrimental increase in the leakage current.[14] It was previously demonstrated that N-doping helps to stabilize the amorphous phase of Ge-based chalcogenides.[15–17] It also
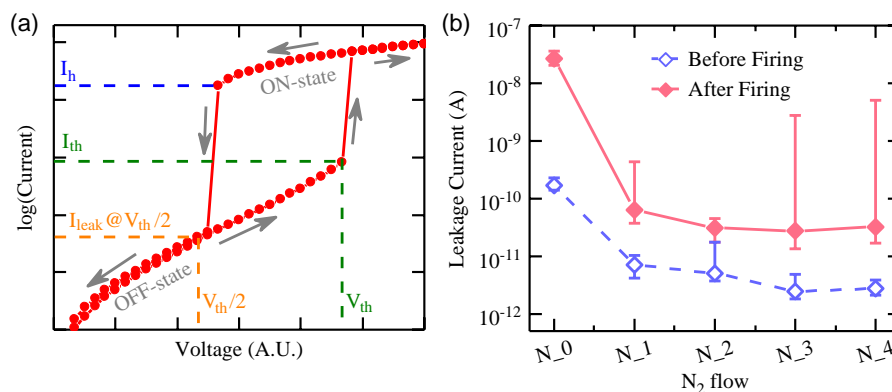
A. Verdy, J.-B. Dory, Dr. G. Navarro, Dr. M. Bernard, Dr. P. Noé
Université Grenoble Alpes, CEA, LETI
F-38000 Grenoble, France
E-mail: anthonin.verdy@cea.fr; gabriele.navarro@cea.fr; pierre.noe@cea.fr

Dr. F. d'Acapito
CNR-IOM-OGG c/o ESRF – The European Synchrotron
71 rue des Martyrs, F-38043 Grenoble, France

The ORCID identification number(s) for the author(s) of this article can be found under https://doi.org/10.1002/pssr.201900548.

1900548 (1 of 7)

**ADVANCED
SCIENCE NEWS**

www.advancedsciencenews.com

pssrrl

physica status solidi

www.pss-rapid.com

Figure 1. a) I–V characteristic of an OTS device describing the switching from the low-field highly resistive OFF-state to the highly conductive ON-state when the applied voltage exceeds the threshold voltage/current value (V_{th}/I_{th}). After the switching, when the applied voltage is decreased below V_{th}, the ON-state can be maintained down to the holding current (I_h), at which the material recovers its highly conductive OFF-state. The leakage current I_{leak} is defined as the current value measured at a voltage equal to $V_{th}/2$. b) Evolution of the leakage current values and their dispersion from the median value measured on OTS devices (see Experimental Section) for different N contents labeled as a function of the N_2 gas flow used in Ar/N_2 plasma of the reactive sputtering deposition process of the OTS thin films. The introduction of N in $Ge_{24}Se_{56}Sb_{20}$ films allows decreasing the leakage current. Furthermore, using an appropriate N content permits to obtain OTS devices exhibiting very low dispersion of the leakage currents, whereas high N contents are characterized by a broad dispersion toward high leakage current (see text).

induces an increase in the bandgap,[16,18] leading to a beneficial decrease in the leakage current.[14,19]

In that context, in addition to the incorporation of N in Ge–Se–Sb films permitting to increase the amorphous phase stability, we evidence its beneficial impact on reducing the leakage current in $Ge_{24}Se_{56}Sb_{20}$ (GSS) film. Finally, we discuss the link between such device performances and the amorphous structure of GSS films exhibiting different N concentrations.

OTS selector devices require a first initialization step called "firing." This first switching event occurs at a higher voltage value (fire voltage or V_{fire}) than the one used in all following switching operations (threshold voltage or V_{th}). The evolution of V_{fire} and V_{th} as a function of N-doping is plotted in Figure S1, Supporting Information. Moreover, an increase in I_{leak} is observed after the firing. Figure 1b shows the evolution of the leakage current measured at $V_{th}/2$ before (i.e., on as-fabricated pristine device) and after firing (i.e., after the application of the first electrical pulse) for $Ge_{24}Se_{56}Sb_{20}$ (GSS) thin films as a function of N concentration labeled as N_x, being x representative of the N_2 gas flow used in Ar/N_2 plasma of the reactive sputtering deposition process (see also the I–V characteristics plotted in Figure S2, Supporting Information). The GSS film free of N exhibits a pristine leakage current of about 10^{-10} A that drastically increases more than two orders of magnitude up to 10^{-8} A after the firing. When N is incorporated in GSS, we observe a reduction in the pristine leakage current below 10^{-11} A and an increase of only about one order of magnitude of the postfiring leakage current. However, whereas the variability of the leakage current values of pristine devices is low, with data almost distributed all around the median, N doping in GSS films seems to induce an important increase in the dispersion on the postfiring leakage currents with a large spread toward the high current values. Indeed, for high N content, we observe a large spread of the data over three orders of magnitude. However, for a specific N content (N_2) in GSS film, low leakage current values with

low variability are observed, even after firing. Thus, even if N doping is beneficial for the improvement of the thermal stability and the reduction in the leakage current, the N content has to be carefully dosed. To get a better insight on such phenomenon, we performed a detailed analysis on the impact of N incorporation on the amorphous structure of GSS films.

To understand the role of N-doping in GSS, the amorphous structure of GSS films with different N contents was investigated using Raman, infrared, and EXAFS spectroscopies. All these complementary techniques are powerful tools to easily get information on the local structure and the bonding configuration inside the amorphous material. **Figure 2**a shows the Raman spectra measured on GSS films as a function of the N content (see the Experimental Section). N-free GSS film is characterized by the Raman modes of Ge–Se and Sb–Se bonds. The Ge–Se Raman modes are located at 200 and 215 cm^{-1} corresponding to Ge–Se vibration in corner- and edge-sharing $GeSe_{4/2}$ tetrahedrons, respectively.[20–23] The Raman modes of Sb–Se bonds appear at 190 cm^{-1} and correspond to Sb–Se vibrations in $SbSe_{3/2}$ pyramids.[21,24] Moreover, an intense mode around 160 cm^{-1} is also observed and can be attributed to Sb–Sb bonds in Se_2Sb–$SbSe_2$ ethane-like motifs.[21,24] When N is incorporated in GSS, this Sb–Sb mode progressively vanishes. When the N_2 composition is reached, the Sb–Sb shoulder at 160 cm^{-1} is not further visible, but for higher N content, a mode near 260 cm^{-1} progressively appears and can be attributed to Se–Se vibrations.[20,22]

In Figure 2b, the Fourier-transform infrared spectroscopy (FTIR) spectra of the different GSS films acquired in the Ge–N absorption range (see the Experimental Section) are shown. Surprisingly, when N is incorporated in GSS, a broad absorption band with multiple contributions located at $\approx$650 and $\approx$750 cm^{-1} appears and progressively increases with the N content. It must be emphasized here that this double absorption peak does not perfectly match with the expected single
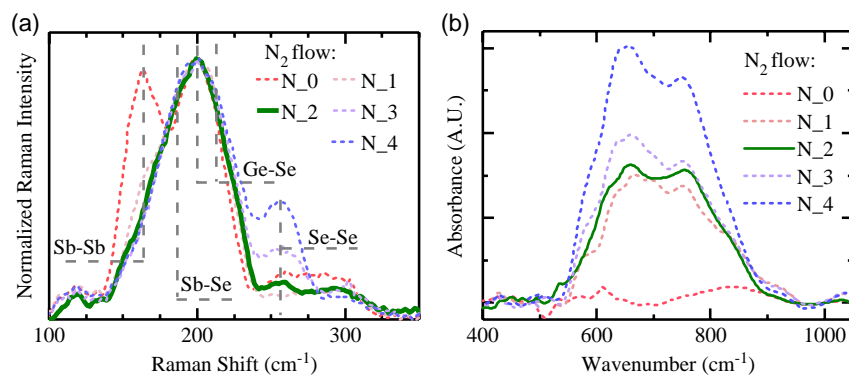
Figure 2. a) Raman spectra of N-doped Ge–Se–Sb films for different N contents labeled as a function of the N_2 gas flow used in Ar/N_2 plasma of the reactive sputtering deposition process. The main modes are reported in the figure. The main contributions correspond to Ge–Se and Sb–Se modes in $GeSe_{4/2}$ tetrahedrons and $SbSe_{3/2}$ pyramids, respectively. Compositions with a low N content exhibit Raman signature of Sb–Sb homopolar bonds, whereas for a high N content, Se–Se bonds appear. For a specific N concentration (GSS-N_2), neither homopolar Sb–Sb nor Se–Se bonds are observed in the Raman spectra. b) FTIR spectroscopy acquired on the Ge–Se–Sb–N OTS thin films. The FTIR spectra are centered on the region of Ge–N absorption bands. After N introduction in the Ge–Se–Sb films, Ge–N bonds are formed with absorption modes centered around $700 \, cm^{-1}$. The nonzero absorbance visible on the N-free Ge–Se–Sb film is a residual signal resulting from imperfect subtraction of contributions of the Si substrate and the 20 nm thick SiN capping layer (see the Experimental Section).

contribution usually observed near $700 \, cm^{-1}$ for amorphous GeN_x films.[25–27] In our case, the splitting of the main FTIR absorption band can be the result of the presence of different environments around the localized Ge–N bonds and GeN_x motifs in the amorphous matrix. Indeed, ab initio simulations predicted that the local atomic configuration around N atoms in N-doped amorphous GeTe phase-change materials' thin films consists of two main structural motifs (NGe_3 pyramids and NGe_4 tetrahedrons) at the origin of two slightly separated absorption bands.[28] However, the experimental FTIR spectra of N-doped GeTe films do not exhibit such bimodal contribution. This could be the result of the slight discrepancy generally observed in the amorphous structure between N-doped GeTe films obtained by sputtering deposition and the melt-quenched glasses of the simulations.[29] Nevertheless, the presence of different atomic environments has also been studied in N-doped $Ge_2Sb_2Te_5$ films, in which a Ge nitride phase separation occurs when nitrogen is incorporated, leading to the formation of two amorphous phases.[30] It is also demonstrated that this phase separation appears predominantly for high N-content. Such an observation is in accordance with our FTIR spectra for which the two contributions of the bimodal IR absorption peak become more well defined as the N content is increased.

To get more information on the local order in our amorphous materials, the films were analyzed by grazing incidence X-ray absorption spectroscopy (GIXAS) acquired at the Ge, Se, and Sb K-egdes (see the Experimental Section). The EXAFS spectra and the corresponding FTs of N-doped and undoped GSS layers extracted from the XAS acquisitions are shown in **Figure 3** (see the Experimental Section for raw data treatment procedure, details on fitting procedure for the quantitative analysis of EXAFS, and Figure S3, Supporting Information, for fitting curves as well as Table S4, Supporting Information, for quantitative results on atomic neighbors, coordination numbers (CNs), and interatomic distances). As shown in Figure 3b and Table S4, Supporting Information, the EXAFS data clearly confirm the

presence of Ge–Se and Sb–Se bonds at $R_{Ge-Se} \approx 2.39 \, Å$ and $R_{Sb-Se} \approx 2.64 \, Å$ in the GSS films, as well as the presence and increasing number of Ge–N bonds at $R \approx 1.84 \, Å$ after N incorporation. However, XAS analysis also shows the presence of Ge–Sb bonds at $R_{Ge-Sb} \approx 2.64 \, Å$ in the GSS film, not visible in Raman and IR characterizations, as well as the possible formation of Sb–N bonds at $R_{Sb-N} \approx 2 \, Å$ when N is incorporated in the GSS matrix. These results are in good agreement with previous EXAFS, neutron diffraction, and X-ray diffraction study on Ge–Se–Sb materials.[31] From the point of view of CNs, quantitative EXAFS analysis follow approximately the so-called Mott rule generally used as reference in such systems.[32] The slight deviations could be attributed to the limit of the accuracy of the Mott rule (that predicts the total CN of an element as 8N, N being the number of s and p electrons in the valence shell of the considered element) as well as to the unavoidable noise in the fluorescence collected data and correlations between amplitude parameters (N and σ). It is noted that in XAS, it is not possible to distinguish X–Se from X–Ge scattering paths, as the electronic density of Ge and Se atoms being too close. Thus, the considered environments are Se–(Ge/Se) and Sb–(Ge/Se). EXAFS measurements confirm the presence of Sb–Sb bonds as well as Sb–(Ge/Se) bonds.

Due to a more favorable enthalpy of formation, Se atoms are preferentially linked to Ge atoms than to Sb atoms in GSS.[33] Our GSS films ($Ge_{24}Se_{56}Sb_{20}$) are chalcogen-deficient compared with $GeSe_2$ and Sb_2Se_3 stoichiometric compositions and with compounds lying on the $GeSe_2$–Sb_2Se_3 pseudobinary tie line. As a result, in our Se-deficient and Sb-rich GSS films, Sb–Sb bonds are thus promoted and appear in ethane-like Se_2Sb–$SbSe_2$ motifs as observed in Raman spectra at $160 \, cm^{-1}$. Moreover, the absence of shoulder or peak in Raman spectra near $140 \, cm^{-1}$ corresponding to the main Raman mode of amorphous a-Sb phase[34] indicates that there is no segregation or formation of a-Sb phase or Sb clusters in GSS film. However, since Raman modes of Ge–Se and Sb–Se expected respectively
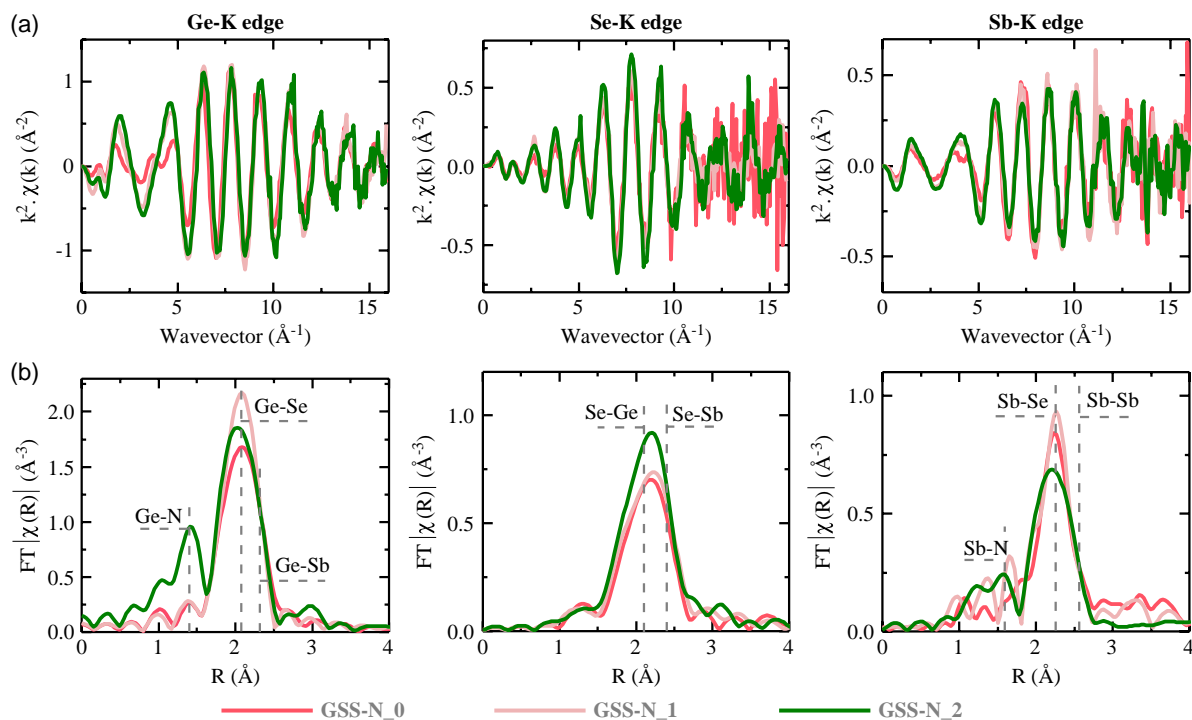
ADVANCED
SCIENCE NEWS
www.advancedsciencenews.com

pss rrl
physica status solidi
www.pss-rapid.com

Figure 3. a) Room temperature k^2-weighted EXAFS spectra and b) their FT acquired at Ge, Se, and Sb K-edges on N-doped $Ge_{24}Se_{56}Sb_{20}$ thin films deposited with N_2 gas flow varying from N_0 to N_2. The position of interatomic distances in the FT for the Ge–Se (Se–Ge), Sb–Se (Se–Sb), Ge–N, and Sb–N bonds is indicated by vertical dashed lines.

at 200 and 190 cm^{-1} are very close, it is difficult to confirm the presence of Sb–Se bonds only on the basis of the Raman spectra. EXAFS measurements permit to confirm unambiguously the presence of Sb–Se bonds as well as Sb–Sb bonds in GSS film. Moreover, EXAFS quantitative analysis gives a Sb–Sb coordination number $CN_{Sb-Sb} = 0.8 \pm 0.3$ that is close to 1, confirming its most probable presence in ethane-like Se_2Sb–$SbSe_2$ motifs as observed on Raman spectra rather than in a nanosegregated Sb phase for which significantly higher CN_{Sb-Sb} would be expected.[35] Despite the lower CN of Sb–Sb bonds compared with Ge–Se ones, the intensity of the Sb–Sb Raman mode at 160 cm^{-1} is surprisingly close to the one of Ge–Se modes. This effect could be the result of the higher polarizability of Sb bonds,[36] meaning that the relative intensity is not relevant to quantify the bonds proportion. EXAFS analysis also shows that the excess of Sb tends to create wrong Ge–Sb bonds that are less probable but previously observed when Sb is incorporated in excess in Ge–Sb–Se glasses.[31] Wrong (Ge–Sb) and homopolar (Sb–Sb) bonds are known to significantly affect the electronic density of states (DoS) of amorphous chalcogenides with introduction of band tail and midgap states.[37–40] These defect states have been held responsible for an increase in the subthreshold current I_{leak} due to an increase in the Poole–Frenkel transport.[19,41,42] The increased density of the electronic defect states and the reduction of the energy barrier for the electrons promote the charge hopping and therefore an increase in the electrical conductivity of the OTS material. Moreover, Sb is known to deteriorate the thermal stability of Ge–Se compositions, promoting the segregation and crystallization of Se and Sb–Se phases.[14,43]

This local segregation can be at the origin of the significant increase by several orders of magnitude of the leakage current after the firing, as shown in Figure 1b, and resulting from the important Joule heating that can be expected when the current flows through the device in the ON-state.

The reduction of the number of homopolar Sb–Sb bonds can be achieved by decreasing the Ge content (i.e., increasing the Se concentration), to increase the fraction of Se bonded to Sb. However, Ge being a good glass former in chalcogenide glasses, decreasing the Ge concentration is not suitable for OTS applications because it can lead to a detrimental degradation of the thermal stability of the material. Thus, for this purpose, N-doping is preferable. Indeed, upon increasing the N concentration in GSS films, a progressive formation of Ge–N bonds occurs at the expense of the Ge–Se bonds, as depicted by the decrease of Ge–(Se+Sb) CN. More Se atoms are released and available to form bonds with Sb. This is evidenced in Raman spectra, where the Sb–Sb mode progressively vanishes as the N content in GSS films is increased, as well as in FTIR spectra where the Ge–N absorption band concurrently increases. The same trend is also seen in the EXAFS analysis where all Ge–N, Sb–(Se/Ge) and Se–Sb CNs increase with the N concentration. For the highest N contents, the valence of Sb atoms being fully filled, Se–Se bonds progressively appear in the Raman spectra at 260 cm^{-1}.

From all the above observations, the most interesting feature is that for a specific N content (sample GSS-N_2), no homopolar Sb–Sb nor Se–Se bonds are detected in the amorphous by both Raman and EXAFS spectroscopies. The reduction in detrimental Sb–Sb and Ge–Sb electronic defect bonds thanks to N-doping

leads to a decrease in the pristine leakage current below 10^{-11} A for N-doped GSS samples, which represents a reduction in more than one order of magnitude compared with undoped GSS. Moreover, after firing, an increase in the leakage current of only about one order of magnitude is observed. We think that beyond the removal of homopolar and wrong bonds, N-doping also increases the glass rigidity and amorphous phase stability thanks to the formation of strong Ge–N and Sb–N covalent bonds. Indeed, it was demonstrated that an optimized N-doped GSS OTS material called GSSN (corresponding to the sample here labeled as GSS-N_2) is able to sustain high-temperature annealing of 400 °C while keeping state-of-the-art OTS performances.[42]

For upper N concentrations (N$_2$ flow > N_2), the formation of Se–Se bonds observed in the Raman spectra does not induce any significant increase in the pristine leakage current measured before the firing, probably thanks to the high bandgap of amorphous selenium of 1.9–2 eV.[44] But, after the firing, such devices exhibit the highest dispersion in leakage current values spreading over two up to three decades (Figure 1b). On the contrary, GSS-N_2, for which there is no evidence of the presence of Se–Se bonds, shows the smallest dispersion of leakage currents, even after the firing. We think that the increase in the dispersion in the samples with high N concentration can be the result of the stochastic formation of localized conductive paths during the firing step. This can result not only from the decrease in the amorphous phase stability induced by Sb incorporation but also from the local formation of metallic Se[45] clusters or chains in the films. Indeed, the thermal stress induced by the Joule heating effect, occurring when the current flows through the device in the ON state, can boost such phenomenon. Such localized segregation and crystallization in the OTS films can increase randomly the leakage current of the devices after the firing.

The main structural features as a function of the N content in GSS OTS films are shown in **Figure 4** with a plot of the relative change in number of Sb–Sb, Ge–N, and Se–Se bonds derived from the integral of corresponding Raman and IR modes.
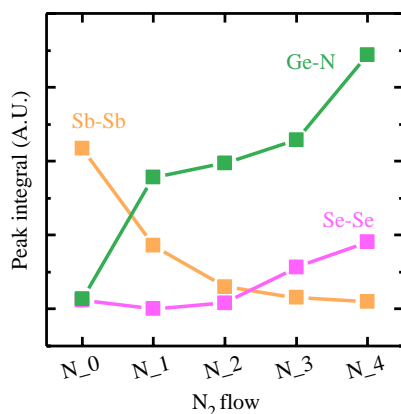
The number of homopolar and wrong bonds reaches its minimum and becomes equal to zero for the optimized GSS-N_2 sample that exhibits the best performance in terms of leakage current values and current dispersion.

To summarize, we studied the link between bonding configurations in amorphous structure of N-doped Ge–Se–Sb chalcogenide thin films and their performances when incorporated in OTS selector devices. A particular emphasis was made on their subthreshold current characteristics currents that are shown to be dependent on the material composition. We demonstrated that the presence of homopolar/wrong bonds in the amorphous OTS materials, mostly Ge–Sb, Sb–Sb, and Se–Se bonds, is detrimental for OTS reliability. In particular, homopolar/wrong bonds such as Sb–Sb or Ge–Sb induce an increase in the leakage current of the pristine OTS devices that is worsened further after the initial firing step. The formation of Se–Se homopolar bonds resulting from a too high N concentration in Ge–Se–Sb–N films has no significant impact on the leakage current of as-fabricated pristine OTS devices but induces a highly dispersed leakage current values after the firing operation. Finally, we demonstrate that the introduction of N in Ge–Se–Sb films is fundamental to avoid undesired bonds. Adjusting the N concentration to form Ge–N and Sb–N bonds permits to remove Sb–Sb and Ge–Sb bonds, responsible for the increase in the leakage current. Nevertheless, for highest N contents, the formation of a high concentration of Ge–N bonds (and in a less extent Sb–N bonds) tends to release Se atoms that can form Se–Se homopolars, leading to the Se segregation that is detrimental for the post-firing OTS leakage current variability. Hence, the optimization of the N concentration in Ge–Se–Sb films allows to drastically limit the presence of homopolar/wrong bonds and enables state-of-the-art OTS devices with very low leakage current, high thermal stability, and lowest device-to-device variability of subthreshold characteristics.

Experimental Section

OTS thin films were deposited by magnetron cosputtering from high-purity $Ge_{30}Se_{70}$ and Sb targets in an industrial cluster tool on 200 mm Si-based substrates. The introduction of N in the Ge–Se–Sb thin films has been achieved by means of reactive magnetron cosputtering under Ar/N$_2$ atmosphere (OTS films are labeled GSS-N_x with × being proportional to the N$_2$ gas flow used in Ar/N$_2$ gas mixture). Film thicknesses, compositions, and deposition homogeneity over the 200 mm substrate were controlled by means of X-ray reflectivity and wavelength dispersive X-ray fluorescence (WDXRF). The thicknesses of the films were fixed to 50 nm for infrared and Raman spectroscopy and 200 nm for XAS/EXAFS measurements. After deposition, all OTS thin-film samples were capped in situ by a 20 nm thick SiN layer without breaking of the vacuum to prevent surface oxidation.

For OTS selector devices fabrication, an OTS layer of a few tens of nanometer was deposited on a top of a 350 nm diameter W plug used as bottom electrode contact. Then, immediately after deposition of the OTS layer, a TiN top electrode was deposited without breaking the vacuum, preventing oxidation of the OTS layer. Leakage currents were measured at $V_{th}/2$ in quasistatic DC mode. Data were collected on 54 devices spatially distributed on the 200 mm substrate. The leakage current values correspond to the median of the distribution, and the dispersion bars represent the values at more or less 34% around the median.

Raman spectra were acquired using a 532 nm laser on a μ-Raman spectrometer. Intensity and exposure time were optimized to avoid any modification of the material under the focused laser beam.

Figure 4. Change in the number of Sb–Sb, Se–Se, and Ge–N bonds as a function of the N$_2$ gas flow used for the reactive deposition of the $Ge_{24}Se_{56}Sb_{20}$ films. The plotted values were obtained by integration of the contribution of the modes in Raman and FTIR spectra (see the Experimental Section). For the optimized GSS-N_2 sample, the number of both Sb–Sb and Se–Se homopolar bonds is close to zero.

FTIR spectroscopy analysis was performed in transmission mode. A sample consisting of only the 20 nm capping layer deposited on a Si substrate was used as reference sample for subtraction of the contributions of Si substrate and SiN layer to the FTIR spectra of OTS thin film samples.

To plot data of Figure 4, Sb–Sb, Se–Se, and Ge–N modes were integrated after deconvolution of the different contributions of Raman spectra for Sb–Sb and Se–Se modes and by integrating all the Ge–N absorption bands of the FTIR spectra.

XAS measurements were conducted at the LISA beamline[46] using a double crystal fixed exit monochromator equipped with Si(111) crystals. In the different campaigns of data collection, harmonic rejection was achieved either by Si-coated ($E_{cutoff} = 15$ keV with incidence angle of 2 mrad) or Pd-coated ($E_{cutoff} = 18$ keV with incidence angle of 3.6 mrad) mirrors for Se–K and Ge–K edges, whereas for Sb–K edge, Pt-coated mirrors ($E_{cutoff} = 40$ keV with incidence angle of 2 mrad) were used. Data were collected at $T = 300$ K in grazing incidence (incidence angle of 0.5°),[47] and the signal was collected in fluorescence mode using a 12 element high-purity germanium detector. Two to four spectra per sample were collected to improve the signal-to-noise ratio.

XAS data were reduced with the ATHENA[48] code and modeled with the ARTEMIS[49] code. Theoretical EXAFS signals were calculated with the FEFF8.1[50] code starting from GaN, InN, GaAs, GaSb structures and the amplitude factors S_0^2 calibrated on experimental data. This choice was dictated from the fact that only for Ga and In, well regular structures are available (wurtzite or zinc blende), and no major effect is expected passing from Ga to Ge or Se and from In to Sb because the central atom and backscattering phase and amplitude functions are practically coinciding due to the similar atomic number. Data at the various K edges of the same sample were fitted simultaneously to minimize the number of free parameters.

Supporting Information

Supporting Information is available from the Wiley Online Library or from the author.

Acknowledgements

Conflict of Interest

The authors declare no conflict of interest.

Author Contributions

P.N. and A.V. conceptualized the study and experiments. M.B. prepared the thin-film samples in LETI clean rooms. G.N. supervised the OTS device fabrication in LETI 200 mm technological platform with help of M.B. A.V. performed and analyzed all the electrical characterization of OTS devices with support of G.N. A.V. performed all Raman and FTIR spectroscopy experiments with support from J.-B.D. and P.N. XAS measurements were conceived by F.d'A. and realized by A.V., J.-B.D., P.N. and F.d'A. The XAS data were analysed by F.d'A. with advices from A.V. and P.N. The article was written by A.V. and P.N. with help of F.d'A. and G.N. All authors have given their approval to the final version of the manuscript.

[1] P. Noé, C. Vallée, F. Hippert, F. Fillot, J.-Y. Raty, Semicond. Sci. Technol. 2018, 33, 013002.

[2] T. Kim, H. Choi, M. Kim, J. Yi, D. Kim, S. Cho, H. Lee, C. Hwang, E.-R. Hwang, J. Song, S. Chae, Y. Chun, J.-K. Kim, in 2018 IEEE Int. Electron Devices Meet., IEEE, 2018, pp. 37.1.1–37.1.4.

[3] G. Navarro, A. Verdy, N. Castellani, G. Bourgeois, V. Sousa, G. Molas, M. Bernard, C. Sabbione, P. Noe, J. Garrione, L. Fellouh, L. Perniola, in 2017 Symp. VLSI Technol., IEEE, 2017, pp. T94–T95.

[4] M. Alayan, E. Vianello, G. Navarro, C. Carabasse, S. L. Barbera, A. Verdy, N. Castellani, A. Levisse, G. Molas, L. Grenouillet, T. Magis, F. Aussenac, M. Bernard, B. DeSalvo, J. M. Portal, E. Nowak, in 2017 IEEE Int. Electron Devices Meet., IEEE, 2017, pp. 2.3.1–2.3.4.

[5] D. Alfaro Robayo, G. Sassine, L. Grenouillet, C. Carabasse, T. Martin, N. Castellani, A. Verdy, G. Navarro, L. Ciampolini, B. Giraud, T. Magis, V. Beugin, E. Vianello, G. Ghibaudo, G. Molas, E. Nowak, in 2019 IEEE Int. Mem. Workshop, IEEE, pp. 132–135.

[6] H. Y. Cheng, W. C. Chien, I. T. Kuo, C. W. Yeh, L. Gignac, W. Kim, E. K. Lai, Y. F. Lin, R. L. Bruce, C. Lavoie, C. W. Cheng, A. Ray, F. M. Lee, F. Carta, C. H. Yang, M. H. Lee, H. Y. Ho, M. BrightSky, H. L. Lung, in 2018 IEEE Int. Electron Devices Meet., IEEE, 2018, pp. 37.3.1–37.3.4.

[7] H. Y. Cheng, W. C. Chien, I. T. Kuo, E. K. Lai, Y. Zhu, J. L. Jordan-Sweet, A. Ray, F. Carta, F. M. Lee, P. H. Tseng, M. H. Lee, Y. Y. Lin, W. Kim, R. Bruce, C. W. Yeh, C. H. Yang, M. BrightSky, H. L. Lung, in 2017 IEEE Int. Electron Devices Meet., IEEE, 2017, pp. 2.2.1–2.2.4.

[8] J. Yoo, Y. Koo, S. A. Chekol, J. Park, J. Song, H. Hwang, in 2018 IEEE Symp. VLSI Technol., IEEE, 2018, pp. 207–208.

[9] N. S. Avasarala, G. L. Donadio, T. Witters, K. Opsomer, B. Govoreanu, A. Fantini, S. Clima, H. Oh, S. Kundu, W. Devulder, M. H. van der Veen, J. Van Houdt, M. Heyns, L. Goux, G. S. Kar, in 2018 IEEE Symp. VLSI Technol., IEEE, 2018, pp. 209–210.

[10] B. Govoreanu, G. L. Donadio, K. Opsomer, W. Devulder, V. V. Afanas'ev, T. Witters, S. Clima, N. S. Avasarala, A. Redolfi, S. Kundu, O. Richard, D. Tsvetanova, G. Pourtois, C. Detavernier, L. Goux, G. S. Kar, in 2017 Symp. VLSI Technol., IEEE, 2017, pp. T92–T93.

[11] S. R. Ovshinsky, Phys. Rev. Lett. 1968, 21, 1450.

[12] A. Verdy, M. Bernard, J. Garrione, G. Bourgeois, M. C. Cyrille, E. Nolot, N. Castellani, P. Noe, C. Socquet-Clerc, T. Magis, G. Sassine, G. Molas, G. Navarro, E. Nowak, in 2018 IEEE Int. Electron Devices Meet., IEEE, 2018, pp. 37.4.1–37.4.4.

[13] S.-Y. Shin, J. M. Choi, J. Seo, H.-W. Ahn, Y. G. Choi, B. Cheong, S. Lee, Sci. Rep. 2015, 4, 7099.

[14] A. Verdy, G. Navarro, V. Sousa, P. Noe, M. Bernard, F. Fillot, G. Bourgeois, J. Garrione, L. Perniola, in 2017 IEEE Int. Mem. Workshop, IEEE, 2017, pp. 1–4.

[15] S. Privitera, E. Rimini, R. Zonca, Appl. Phys. Lett. 2004, 85, 3044.

[16] B. Huang, Phys. Status Solidi B 2015, 252, 431.

[17] A. Fantini, V. Sousa, L. Perniola, E. Gourvest, J. Bastien, S. Maitrejean, S. Braga, N. Pashkov, A. Bastard, B. Hyot, A. Roule, A. Persico,

H. Feldis, C. Jahan, J. Nodin, D. Blachier, A. Toffoli, G. Reimbold, F. Fillot, F. Pierre, R. Annunziata, D. Benshael, P. Mazoyer, C. Vallee, T. Billon, J. Hazart, B. De Salvo, F. Boulanger, in *2010 Int. Electron Devices Meet.*, IEEE, **2010**, pp. 29.1.1–29.1.4.

[18] S. Clima, B. Govoreanu, K. Opsomer, A. Velea, N. S. Avasarala, W. Devulder, I. Shlyakhov, G. L. Donadio, T. Witters, S. Kundu, L. Goux, V. Afanasiev, G. S. Kar, G. Pourtois, in *2017 IEEE Int. Electron Devices Meet.*, IEEE, **2017**, pp. 4.1.1–4.1.4.

[19] N. S. Avasarala, B. Govoreanu, K. Opsomer, W. Devulder, S. Clima, C. Detavernier, M. van der Veen, J. Van Houdt, M. Henys, L. Goux, G. S. Kar, in *2017 47th Eur. Solid-State Device Res. Conf.*, IEEE, **2017**, pp. 168–171.

[20] P. Lucas, E. A. King, O. Gulbiten, J. L. Yarger, E. Soignard, B. Bureau, *Phys. Rev. B* **2009**, *80*, 214114.

[21] Z. G. Ivanova, E. Cernoskova, V. S. Vassilev, S. V. Boycheva, *Mater. Lett.* **2003**, *57*, 1025.

[22] P. Tronc, M. Bensoussan, A. Brenac, C. Sebenne, *Phys. Rev. B* **1973**, *8*, 5947.

[23] K. Jackson, A. Briley, S. Grossman, D. V. Porezag, M. R. Pederson, *Phys. Rev. B* **1999**, *60*, R14985.

[24] E. Baudet, C. Cardinaud, A. Girard, E. Rinnert, K. Michel, B. Bureau, V. Nazabal, *J. Non-Cryst. Solids* **2016**, *444*, 64.

[25] I. Chambouleyron, A. R. Zanatta, *J. Appl. Phys.* **1998**, *84*, 1.

[26] F. C. Marques, I. Chambouleyron, F. Evangelisti, *J. Non Cryst. Solids* **1989**, *114*, 561.

[27] G. Maggioni, S. Carturan, L. Fiorese, N. Pinto, F. Caproli, D. R. Napoli, M. Giarola, G. Mariotto, *Appl. Surf. Sci.* **2017**, *393*, 119.

[28] J.-Y. Raty, P. Noé, G. Ghezzi, S. Maîtrejean, C. Bichara, F. Hippert, *Phys. Rev. B* **2013**, *88*, 014203.

[29] J. Raty, *Phys. Status Solidi RRL* **2019**, *13*, 1800590.

[30] K. B. Borisenko, Y. Chen, S. A. Song, D. J. H. Cockayne, *Chem. Mater.* **2009**, *21*, 5244.

[31] I. Pethes, R. Chahal, V. Nazabal, C. Prestipino, A. Trapananti, S. Michalik, P. Jóvári, *J. Phys. Chem. B* **2016**, *120*, 9204.

[32] N. F. Mott, *Rev. Phys. Appliquée* **1977**, *12*, 619.

[33] A. Dahshan, K. A. Aly, *Philos. Mag.* **2008**, *88*, 361.

[34] J. S. Lannin, *Phys. Rev. B* **1977**, *15*, 3863.

[35] M. Ropo, J. Akola, R. O. Jones, *Phys. Rev. B* **2017**, *96*, 184102.

[36] K. S. Andrikopoulos, S. N. Yannopoulos, A. V. Kolobov, P. Fons, J. Tominaga, *J. Phys. Chem. Solids* **2007**, *68*, 1074.

[37] J. Y. Raty, W. Zhang, J. Luckas, C. Chen, R. Mazzarello, C. Bichara, M. Wuttig, *Nat. Commun.* **2015**, *6*, 7467.

[38] P. Noé, C. Sabbione, N. Castellani, G. Veux, G. Navarro, V. Sousa, F. Hippert, F. d'Acapito, *J. Phys. D: Appl. Phys.* **2016**, *49*, 035305.

[39] J. Luckas, D. Krebs, S. Grothe, J. Klomfaß, R. Carius, C. Longeaud, M. Wuttig, *J. Mater. Res.* **2013**, *28*, 1139.

[40] F. Zipoli, D. Krebs, A. Curioni, *Phys. Rev. B* **2016**, *93*, 115201.

[41] D. Ielmini, *Phys. Rev. B* **2008**, *78*, 035308.

[42] A. Verdy, G. Navarro, M. Bernard, P. Noe, G. Bourgeois, J. Garrione, M.-C. Cyrille, V. Sousa, E. Nowak, in *2018 IEEE Int. Mem. Workshop IMW*, IEEE, **2018**, pp. 1–4.

[43] R. W. Haisty, H. Krebs, *J. Non Cryst. Solids* **1969**, *1*, 399.

[44] A. K. Bhatnagar, K. V. Reddy, V. Srivastava, *J. Phys. Appl. Phys.* **1985**, *18*, L149.

[45] C. H. Champness, R. H. Hoffmann, *J. Non Cryst. Solids* **1970**, *4*, 138.

[46] F. d'Acapito, G. O. Lepore, A. Puri, A. Laloni, F. La Manna, E. Dettona, A. De Luisa, A. Martin, *J. Synchrotron Radiat.* **2019**, *26*, 551.

[47] C. Maurizio, M. Rovezzi, F. Bardelli, H. G. Pais, F. D'Acapito, *Rev. Sci. Instrum.* **2009**, *80*, 063904.

[48] M. Newville, *J. Synchrotron Radiat.* **2001**, *8*, 322.

[49] B. Ravel, M. Newville, *J. Synchrotron Radiat.* **2005**, *12*, 537.

[50] A. L. Ankudinov, B. Ravel, J. J. Rehr, S. D. Conradson, *Phys. Rev. B* **1998**, *58*, 7565.